



# On the Existence of Fast Modes in Compressible Magnetohydrodynamic Turbulence

Zhaoming Gan<sup>1,2</sup> , Hui Li<sup>2</sup> , Xiangrong Fu<sup>1,2</sup> , and Senbei Du<sup>2</sup> <sup>1</sup> New Mexico Consortium, Los Alamos, NM 87544, USA; [zgan@newmexicoconsortium.org](mailto:zgan@newmexicoconsortium.org)<sup>2</sup> Los Alamos National Laboratory, Los Alamos, NM 87545, USA

Received 2021 November 29; revised 2021 December 31; accepted 2022 January 19; published 2022 February 28

## Abstract

We study the existence and properties of fast magnetosonic modes in 3D compressible MHD turbulence by carrying out a number of simulations with compressible and incompressible driving conditions. We use two approaches to determine the presence of fast modes: mode decomposition based on spatial variations only and spatio-temporal 4D fast Fourier transform (4D FFT) analysis of all fluctuations. The latter method enables us to quantify fluctuations that satisfy the dispersion relation of fast modes with finite frequency. Overall, we find that the fraction of fast modes identified via the spatio-temporal 4D FFT approach in total fluctuation power is either tiny with nearly incompressible driving or  $\sim 2\%$  with highly compressible driving. We discuss the implications of our results for understanding the compressible fluctuations in space and astrophysical plasmas.

*Unified Astronomy Thesaurus concepts:* Magnetohydrodynamics (1964); Interplanetary turbulence (830); Alfvén waves (23); Space plasmas (1544); Magnetohydrodynamical simulations (1966)

## 1. Introduction

Magnetized plasma systems, such as magnetic fusion experiments (e.g., Diamond et al. 2005), solar wind (e.g., Matthaeus & Goldstein 1982), interstellar medium (e.g., Armstrong et al. 1995), and intracluster medium (e.g., Hitomi Collaboration et al. 2018), are often turbulent. Magnetohydrodynamics (MHD) is generally employed to describe turbulence in such systems. Understanding the nature of compressible fluctuations is also critical in describing the relationship between the limits of weak and strong turbulence (e.g., Chandran 2005; Galtier 2009, 2018; Meyrand et al. 2016), because the cascade process, anisotropy, and energy spectrum are likely all modified by compressible effects.

The eigenmodes in a compressible MHD system are different from those in the incompressible limit. We choose to focus on fast magnetosonic modes or fast modes in this study. Fast modes are often included in global solar wind models, and are critical in preferential ion heating at kinetic scales through turbulent cascade (e.g., Cranmer & Ballegooyen 2012). They may also play an important role in interpreting the recent Voyager 1 observations (Zank et al. 2017, 2019, 2020; Burlaga et al. 2018). Fast modes have also been used in accelerating particles in solar flares (e.g., Miller et al. 1996) and cosmic rays (e.g., Schlickeiser 2002), and in scattering cosmic rays in the interstellar medium (e.g., Yan & Lazarian 2002). Furthermore, it is postulated that fast-mode turbulence is effective in producing stochastic particle acceleration in various high-energy astrophysical systems as well (e.g., Dermer et al. 1996; Li & Miller 1997; Demidov et al. 2020).

Earlier studies have examined the fraction of compressible modes in MHD turbulence and their cascade properties. The primary method is to use only the *spatial variations* of various variables and decompose them into three eigenmodes—fast, slow, and Alfvén modes (see, e.g., Marsch 1986; Cho & Lazarian 2003; Zhang et al. 2015; Yang et al. 2018). The

effects of turbulence driving conditions have been examined by Makwana & Yan (2020), and they found that the Fourier power in fast modes could be up to  $\sim 30\%$  of the total turbulent power if the turbulence driving is highly *compressible*, and the power in slow modes is even more significant.

Another interesting approach in identifying fast modes in a turbulence simulation was discussed by Svidzinski et al. (2009). They demonstrated that a spatio-temporal analysis method can be used to decompose the fluctuations (say magnetic fields) using a fast Fourier transform (FFT) in both spatial and temporal domains, if a large number of data volumes at different time slices are stored to resolve both low and high frequencies (we will refer to this approach as 4D FFT). Similar approaches have also been applied to simulations of MHD turbulence (e.g., Dmitruk & Matthaeus 2007, 2009; Clark di Leoni et al. 2015; Meyrand et al. 2016; Andrés et al. 2017; Lugones et al. 2019; Yang et al. 2019; Brodiano et al. 2021), as well as in hybrid kinetic simulations (Markovskii & Vasquez 2020). Dmitruk & Matthaeus (2007, 2009) examined spatio-temporal turbulence signals in the incompressible regime. The existence of compressible modes (fast and slow waves) that satisfy dispersion relations in the frequency–wavenumber ( $\omega$  versus  $k$ ) space (e.g., Andrés et al. 2017; Yang et al. 2019) has also been demonstrated. Following these earlier studies, we build similar 4D FFT routines to analyze MHD turbulence. In particular, the recent paper by Brodiano et al. (2021) is most similar to the study presented here. They studied the effects of how compressible versus incompressible driving affects the presence of waves in turbulence. They concluded that the system is mainly dominated by nonlinear fluctuations (i.e., not waves).

In this paper, we aim to address the detailed properties of fast modes in compressible MHD turbulence, particularly the existence of finite-frequency waves and how they vary under different turbulence driving conditions. In Section 2 we describe our simulation setups and various runs we performed. In Section 3 we present our analysis and results of numerical simulations. Conclusions and implications of our results are given in Section 4.



Original content from this work may be used under the terms of the [Creative Commons Attribution 4.0 licence](https://creativecommons.org/licenses/by/4.0/). Any further distribution of this work must maintain attribution to the author(s) and the title of the work, journal citation and DOI.

## 2. Model Description

### 2.1. Numerical Schemes

To address the existence and properties of fast modes in compressible MHD turbulence, we solve the time-dependent ideal MHD equations numerically in a three-dimensional Cartesian coordinate system  $(x, y, z)$  using the code `ATHENA++` (Stone et al. 2020). We introduce  $\mathbf{f}_v$  and  $\mathbf{f}_B$  terms in the momentum and induction equations as turbulence driving forces on velocity and magnetic fields, respectively. Both  $\mathbf{f}_v$  and  $\mathbf{f}_B$  take the form of  $\mathbf{A} \sin(\mathbf{k} \cdot \mathbf{x} + \phi)$  across the computational domain with wavenumbers  $\mathbf{k}$  that satisfy a periodic boundary, and randomly selected phases  $\phi$ , and amplitudes  $\mathbf{A}_v$  and  $\mathbf{A}_B$  for velocity and magnetic fields, respectively. The amplitude is decomposed into components parallel and perpendicular to the background magnetic field  $\mathbf{B}_0$  as  $\mathbf{A}_\parallel$  and  $\mathbf{A}_\perp$ . For velocity driving, we further define a free parameter  $f_c$  as  $|\mathbf{A}_\parallel| = |\mathbf{A}_\perp| \times f_c / (1 - f_c)$  so that  $f_c = 0$  and  $f_c = 1$  represent the incompressible and fully compressible driving limits, respectively. All runs have uniform background density and magnetic fields in which we choose our normalization as  $\rho_0 = 1$  and  $\mathbf{B}_0 = [8, 0, 0]$ , so the characteristic Alfvén speed is  $v_A = 8$ . We use an isothermal equation of state. The initial mean velocity is set to 0, and for all runs, we set a uniform initial sound speed  $c_s = \sqrt{p/\rho}$  using  $\beta = 8\pi p/B^2 = 0.4$ . We apply random driving that follows the Ornstein–Uhlenbeck process with a correlation time  $t_{cor} = 0.5\tau_A$  (Eswaran & Pope 1988), where  $\tau_A = L_0/v_A$  with  $L_0$  being the box size along  $\mathbf{B}_0$ . All driving and/or injection occurs at specific wavenumbers that have  $0 < |\mathbf{k}_{inj}| \leq 2$ . The range of turbulent Mach number  $M_{turb} \equiv \delta v/c_s$  is between 0.12 and 0.18 for the simulations discussed here.

### 2.2. Mode Decomposition Methods

We describe two methods to identify various wave modes in turbulence. The first one is the “spatial-only” method described in Cho & Lazarian (2003) and Yang et al. (2018), which uses the velocity output at each time frame to identify the fractions of Alfvén, fast, and slow modes, according to the polarization features of velocity predicted by linear wave theory. This approach relies on the fact that any spatial variations at any given time frame can be projected onto three eigenvectors *mathematically*. The physical interpretation of this approach, however, is a bit unclear. It certainly makes sense physically when the fluctuation amplitudes are small and nonlinear interactions among different modes are not dominant. But for strong MHD turbulence, the nonlinear interactions become important. It is unclear whether this approach alone can be used to determine the fractions of various wave components.

The other method we used is the spatio-temporal Fourier transform (4D FFT), which allows us to obtain both spatial and frequency information on variations. By storing the data outputs frequently with sufficient time resolution ( $\sim 100$  frames within each  $\tau_A$  up to  $\sim 10\tau_A$ ), we are able to resolve the dispersion relation of linear waves. This ensures that both the high and low frequencies are captured (they are also related to the spatial resolution and box size). To reduce the data volume, we split the 4D Fourier transform into two steps. First, we make a 3D spatial FFT for a variable (e.g., velocity), and store the intermediate data in a time series. Second, we perform the fourth (temporal) layer of the spatio-temporal Fourier transform (for individual frequencies) by integrating the intermediate data

over time, and save the results in a series of individual frequencies for further analysis. The outcome of these analyses will be spectral power populated within the 4D  $\omega$ – $\mathbf{k}$  volume. This approach has the advantage of assessing whether the fast, slow, and Alfvénic fluctuations indeed satisfy their respective dispersion relations.

The three eigenmodes delineate three isosurfaces in the  $\omega$ – $\mathbf{k}$  volume. To determine whether a certain spectral power belongs to a specific eigenmode, we allow  $\pm 10\%$  deviation in  $\omega$  for a specific  $\mathbf{k}$  to compensate for two effects. First, there is the well-known issue of spectral leakage in a Fourier transform when periodic signals are truncated unevenly (Harris 1978), which is the case in the temporal dimension. (We employ periodic boundaries in the spatial dimensions.) To suppress the spectral leakage, the Hanning window function is used in the temporal dimension. Second, there is the possible frequency broadening due to nonlinear interactions. We have also tried to use other “widths” of  $\pm 3\%$  and  $\pm 40\%$ , but the main conclusions do not change qualitatively.

## 3. Results

We present results from three runs A, B, and C that differ in their turbulence driving: both A and C have only velocity driving ( $\mathbf{f}_v$ ) but A has incompressible driving ( $f_c = 0$ ) while C has highly compressible driving ( $f_c = 0.9$ ). Run B has  $f_c = 0$ , but with both  $\mathbf{f}_v$  and  $\mathbf{f}_B$ . All simulations use  $512^3$  resolution. Both A and C have a cubic simulation box of size  $2\pi \times 2\pi \times 2\pi$ , and B has an elongated box of size  $8\pi \times 2\pi \times 2\pi$ . All analyses are performed after simulations have reached a quasi-steady state, typically after several  $\tau_A$ .

First, we show the outcome of 4D FFT analyses in identifying various waves as depicted in Figure 1. Panel (a) shows the spatio-temporal spectrum of run B with an elongated box in a 3D representation of  $\omega$  versus  $k_x$  and  $k_y$ , with  $k_z = 0$  for this plot. We note that  $k_\parallel \simeq k_x$  and  $k_\perp \simeq (k_y^2 + k_z^2)^{1/2}$ . It is clear that fluctuations have cascaded to higher  $k$  and with finite frequency. Several main features can be identified. The theoretical dispersion planes are marked as gray surfaces for fast, Alfvén, and slow modes. The vertical feature along the  $\omega$  axis at small  $|\mathbf{k}| \leq 2$  is due to driving. Panel (b) shows a 2D cut with  $k_x = 0$ , in which the fast mode is most easily identified, given its finite frequency. In this limit, both Alfvén and slow modes have zero frequency. Panel (c) shows another 2D cut with  $k_\perp = 5$ . This brings out all three wave branches (as marked by the three white lines). Panel (d) shows the power distribution in the  $k_\parallel$ – $k_\perp$  plane by integrating the spectrum over all frequencies. This distribution is similar to the previous studies that demonstrate the anisotropic cascade in  $k$ -space (e.g., Chhiber et al. 2020). Note that in panels (b), (c), and (d) we have integrated all possible combinations of  $k_y$  and  $k_z$  for a given  $k_\perp$  to capture all the spectral power.

It is interesting to see that there is a limited amount of power (to be quantified later) in fluctuations that cascade to both higher  $k$  and higher  $\omega$  and satisfy the dispersion relations for the three eigenmode branches, as most easily seen in panels (c) and (b). Slow modes tend to cascade further in  $k$  than both the Alfvén and fast modes, as corroborated by panel (a).

The most prominent feature is the large fraction of fluctuation power *not* on any of the three wave branches, which is clearly shown in the lower right region in panel (b) and the regions in-between three wave surfaces in panel (a). These fluctuations contain finite  $\mathbf{k}$  and finite  $\omega$  even though the

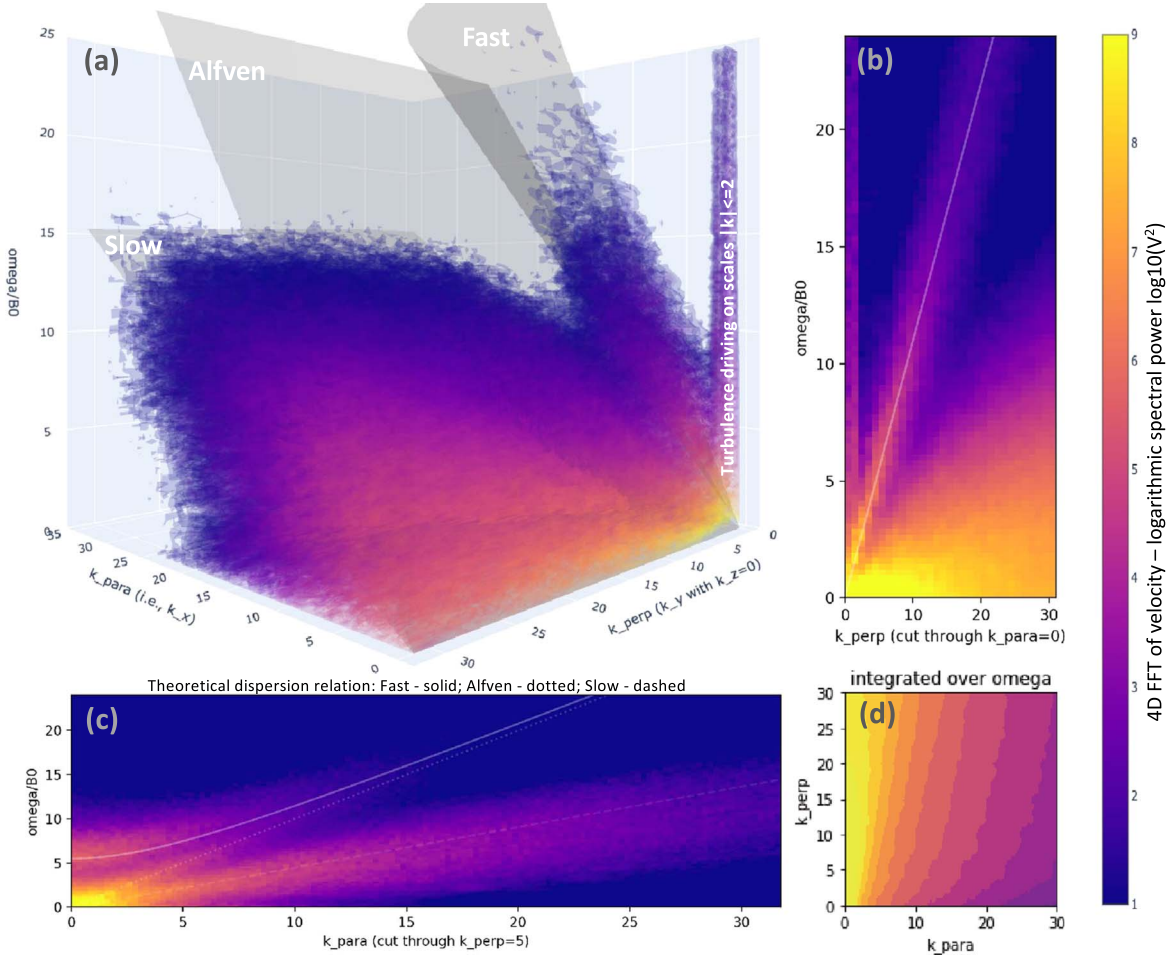


**Figure 1.** Spatio-temporal (4D FFT) spectrum of run B in the  $\omega$  vs.  $k_{\perp}$  and  $k_{\parallel}$  domain, showing the fast, Alfvén, and slow components that are indicated by the gray surfaces shown in panel (a), as well as fluctuations we call “non-waves.” 2D cuts are shown in panels (b) and (c) to emphasize the three wave branches and the non-wave component. Panel (d) depicts the power distribution in the  $k_{\parallel}$ - $k_{\perp}$  plane by integrating the spectrum over all frequencies.

highest concentration of power tends to be in the low- $\omega$  region. We call them the “non-wave” component, which, judging from these plots, contains the most power. By inference, most of the power contained in the  $k_{\perp}$  cascade shown in panel (d) resides in this “non-wave” component as well.

Second, we quantify the percentage of spectral power in various components using runs A, B, and C, when the evolution of each run has reached a quasi-steady state (after  $7-10\tau_A$ ). Because it is uncertain how to interpret the power associated with the injection  $k$ -space, we adopt two approaches. The first is to use outputs including the injection phase space and calculate the percentage of various components using the spatial-only method. We find that the fractions of Alfvén/fast/slow (or A/F/S) for runs A, B, and C are: 0.760/0.017/0.223 (A), 0.628/0.028/0.344 (B), and 0.400/0.206/0.394 (C), respectively. These are represented as the (shaded) left bars in Figure 2. Both the dominance of Alfvén modes and the increasing fraction of fast modes with compressible driving are consistent with the previous studies (e.g., Makwana & Yan 2020).

The other approach we used is to exclude certain regions in  $k$ -space, then use both the spatial-only and the 4D FFT methods to calculate the power fraction in each component. In order to avoid ambiguity, we exclude the following parts from our percentage analysis. First, because the injection  $k$  range is

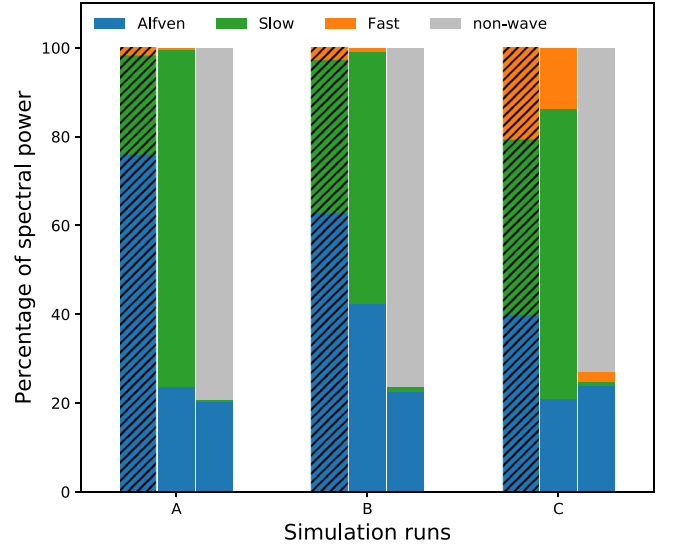


**Figure 2.** Percentage of spectral power derived from the spatial-only mode decomposition (left and middle bars) and spatio-temporal spectra (right bars) for runs A, B, and C. The (shaded) left bars use the whole data cubes, while the middle and right bars use data cubes with some regions excluded (see text for details). With the spatio-temporal spectra method, the non-wave component is dominant and the fast mode fraction is very small (right bars).



dominated by the injection process, we will exclude fluctuation power with  $|k| \leq 2$  in all analysis. In run B, this is  $\sim 70\%$  of the total spectral power in the simulation. In addition, we also exclude fluctuations with  $k_{\parallel} = 0$  and  $\omega = 0$  due to the degeneracy of Alfvén and slow modes. This is  $\sim 3\%$  of the total power. After these modifications to the data outputs, in Figure 2 we compare those derived from the spatial mode decomposition method (middle bars) and spatio-temporal spectrum method (right bars). For the spatial decomposition method, we find the following: the A/F/S fractions are 0.237/0.003/0.760 (A), 0.425/0.007/0.568 (B), and 0.210/0.137/0.653 (C), respectively. The slow mode actually has the largest fraction among three wave modes using the spatial decomposition method. This is different from the previous results by other groups probably because we excluded the injection range. The fast mode fraction, being 0.3% for run A and 0.7% for run B, is negligible when the driving is incompressible but becomes a noticeable fraction of 14% in run C when the driving is highly compressible, which is expected.

For the 4D FFT approach, we identify various wave branches according to the theoretical dispersion relations, and we allow 10% deviation in the theoretical frequencies above/below the gray wave surfaces in Figure 1(a) for each wave branch. The remaining power that does not fit within any of the three branches is considered as non-wave. Quantitatively, the percentages of these four components non-wave/A/F/S are  $0.792/0.204/1 \times 10^{-4}/0.003$  (A),  $0.762/0.225/8 \times 10^{-7}/0.013$  (B), and  $0.729/0.238/0.024/0.009$  (C), respectively. They show that the non-wave component is dominant. With regard to wave modes, the Alfvén component has the largest fraction. The fast mode component is negligible for both A and B but reaches  $\sim 2.4\%$  for C.

One key conclusion demonstrated in Figure 2 is that, while the spectral power can *always* be decomposed into one of three “wave” modes using the spatial decomposition method, when taking into account their frequency behavior, most of these fluctuations do not follow any dispersion relation. Figure 2 also shows that the total fraction in waves using the 4D FFT method is less than  $\sim 25\%$ . Run B is designed to have the most Alfvénic component by including magnetic injection. Indeed, for both methods, the Alfvén mode fraction is higher in B than in either A or C. This driving also generates a finite, albeit small, fraction of slow waves in run B. Run C is designed to have the most compressible modes, but its fast mode fraction decreases from  $\sim 14\%$  using the spatial decomposition method to  $\sim 2.4\%$  using the 4D FFT method.

To test the dependence on the choice of frequency “width,” we also calculate the percentages of spectral power by capturing the power within  $\pm 3\%$  and  $\pm 40\%$  of the theoretical frequency, using data cubes with exclusions as described above. These are summarized in Figure 3. The non-wave/A/F/S components are: for  $\pm 40\%$ , 0.727/0.218/0.005/0.050 (A), 0.590/0.289/ $7 \times 10^{-6}$ /0.121 (B), and 0.535/0.283/0.080/0.102 (C); for  $\pm 3\%$ , 0.795/0.204/ $1 \times 10^{-4}$ / $8 \times 10^{-4}$  (A), 0.773/0.224/ $2 \times 10^{-7}$ /0.003 (B), and 0.749/0.236/0.011/0.002 (C), respectively. It can be seen that the overall trends do not change as we vary from  $\pm 3\%$  to  $\pm 40\%$ .

Third, we examine the second-order structure function of various components to further quantify their properties. We calculate the structure functions of individual components in run B obtained using the two mode decomposition methods and use 3% frequency width.

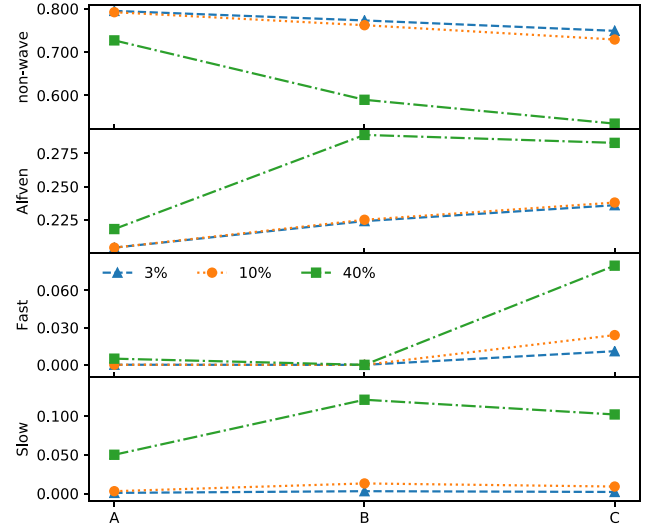


**Figure 3.** Fractions of spectral power for non-wave, Alfvén, fast, and slow components (from top to bottom), for runs A, B, and C. These are obtained using the spatio-temporal method only.

Figure 4 shows the contours of the second-order structure function from run B using the spatial-only mode decomposition (top) and the 4D FFT method (bottom). For the top row, we split the Fourier spectral power of the total velocity into fast, Alfvén, and slow modes. Then we make the inverse Fourier transform and calculate the second-order structure function of these three modes in real space. Fast modes tend to be isotropic, while Alfvén and slow modes are elongated, consistent with previous studies (Goldreich & Sridhar 1995; Cho & Lazarian 2002, 2003). To avoid double-counting, we exclude the fluctuations with  $k_{\parallel} = 0$  (where Alfvén and slow modes are degenerate) and  $k_{\perp} = 0$  (where Alfvén and fast modes are degenerate). For the bottom panel, we first identify various wave branches according to the theoretical dispersion relation, allowing 3% deviation in the theoretical frequencies above/below the gray wave surfaces in Figure 1(a) for each wave branch. Then we make a 4D inverse Fourier transform and calculate the structure functions for the non-wave, fast, Alfvén, and slow components, as shown in the contour plots. We see the general trend that the fast mode appears more isotropic, and the other three components are more anisotropic. (The slow component might be too noisy to be accurate.)

To further quantify the differences in wave components derived from the two methods, in Figure 5 we plot the relationship  $L_{\parallel} \propto L_{\perp}^q$  of various components identified in runs B and C. We summarize the power index  $q$  as follows: run B spatial-only, total/A/F/S =  $\frac{2}{3}/\frac{2}{3}/1/\frac{2}{3}$ ; run B 4D FFT, non-wave/A/F/S =  $\frac{2}{3}/1/1/1$ ; run C spatial-only, total/A/F/S =  $\frac{5}{6}/\frac{2}{3}/\frac{4}{5}/\frac{2}{3}$ ; run C 4D FFT, non-wave/A/F/S =  $\frac{5}{6}/\frac{2}{3}/1/1$ . (Note that we have added the results for run C using the spatial-only method.)

Taking Figures 4 and 5 together, we can tentatively draw the following conclusions. (1) Using the spatial-only method with incompressible driving, the relations  $L_{\parallel} \propto L_{\perp}^{2/3}$  for the total, Alfvén, and slow components, and  $L_{\parallel} \propto L_{\perp}$  for the fast component, are the same as those given by previous studies (e.g., Cho & Lazarian 2003). (2) Using the spatial-only method but with highly compressible driving, the slopes for the total (5/6) and fast mode (4/5) components are actually slightly different from the incompressible case (2/3 for total and 1 for fast). (3) Using the

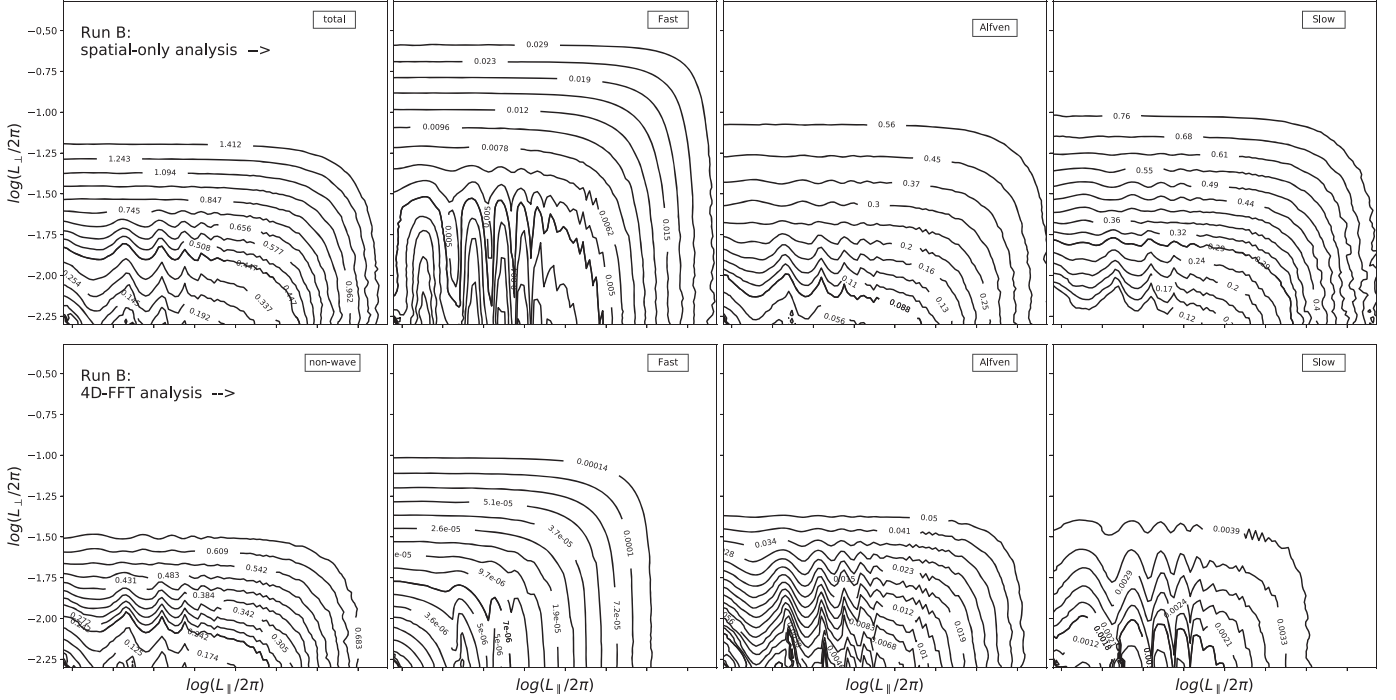


**Figure 4.** Contours of the second-order structure function of velocity for run B, separately calculated using different components, using the spatial decomposition analysis (top) and the 4D FFT analysis (bottom).

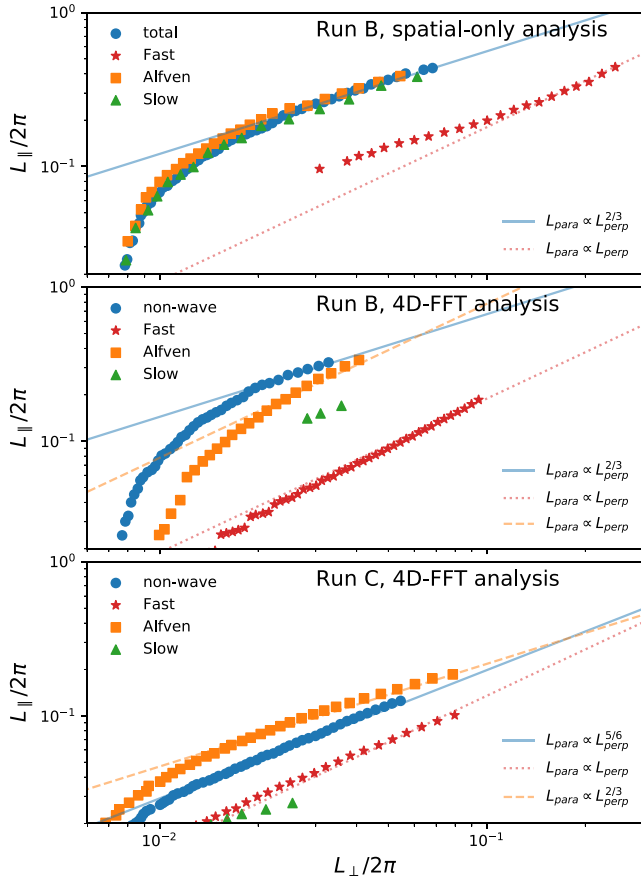


**Figure 5.** Relationships between  $L_{\perp}$  and  $L_{\parallel}$  for different components identified in run B (spatial decomposition only), run B (4D FFT method), and run C (4D FFT method).

4D FFT method, for A/F/S components, both runs B and C give either the same or slightly steeper slopes than those obtained via the spatial-only method. (4) Using the 4D FFT method, there are differences in the slopes for the non-wave and Alfvén components when comparing runs B and C. (5) The fast component using the 4D FFT method gives a slope of 1 for both runs B and C. (6) As a consistency check, for both runs B and C, the slopes for the total and for the non-wave component are the same ( $2/3$ ,  $5/6$ ) because they dominate the spectral power using either the spatial-only or the 4D FFT method. These slopes, showing slight variations under different conditions, suggest that additional theoretical and numerical studies are needed to address these differences.

#### 4. Conclusion and Discussion

To understand the nature of MHD turbulence fluctuations in the frequency versus wavenumber domain in more detail, we have applied both the spatial decomposition method and the spatio-temporal method to examine the properties of MHD turbulence. In particular, we present results from three simulations, one (run A) with incompressible velocity driving, one (run C) with highly compressible velocity driving, and one (run B) with incompressible velocity and magnetic field driving.

After excluding fluctuations associated with driving and the ( $k_{\parallel}=0$ ,  $\omega=0$ ) component, we find that: when taking into account the frequency behavior, the majority of the fluctuations cannot fit within any of the Alfvén, fast, and slow mode branches. We call them the “non-wave” component, and they account for about 75%–80% of the total power. Furthermore, we find that most of the “non-wave” power is of low frequencies. Similar findings of ultralow-frequency spectral power were presented in Dmitruk & Matthaeus (2007, 2009), i.e., their “ $1/f$  noise.” However, to resolve the “ $1/f$  noise” in 4D FFT analysis may require an even longer time duration and a larger simulation domain than what we used here, which is beyond the scope of this

paper. Observationally, the strong non-wave component is consistent with the results of Bieber et al. (1996) and subsequent work that showed the solar wind admits frequently an 80%–20% decomposition into 2D-slab modes. Theoretically, the nearly incompressible models of MHD predict (for plasma beta  $\sim 1$  or  $\ll 1$ ) a dominance of 2D over slab fluctuations (Zank & Matthaeus 1992, 1993; Zank et al. 2017, 2020).





For those fluctuations that fit within one of the wave branches, the Alfvén mode dominates. The fast mode is essentially negligible in runs with incompressible driving, and becomes  $\sim 2.4\%$  in the run with the highly compressible driving (see, e.g., Zhao et al. 2021, for the minority of fast modes in observations).

In addition, we find that the second-order structure functions for different components show differences from those obtained based on the spatial decomposition method.

Because the fast modes in MHD turbulence have been postulated to play an important role in understanding particle transport and energization, our results here should open up new questions on the existence of these fast modes and what quantitative roles they could play. Using the spatial decomposition method to identify different wave modes might be too optimistic in concluding the fraction of fast modes (and compressible modes in general). Instead, we suggest that the “non-wave” component needs to be taken into account in the particle transport and energization processes in MHD turbulence. This will be a subject of our future studies.

We acknowledge the support from a NASA/LWS project under award No. 80NSSC20K0377 and 80HQTR20T0027. H.L., S.D., and X.F. also acknowledge the support by DOE OFES program and LANL LDRD program. Useful discussions with X. Li and F. Guo are gratefully acknowledged. Simulations were carried out using LANL’s Institutional Computing resources. Part of the data analysis was performed on the supercomputer Frontera provided by the Texas Advanced Computing Center (TACC) at The University of Texas at Austin.

### ORCID iDs

Zhaoming Gan  <https://orcid.org/0000-0003-3886-0383>  
 Hui Li  <https://orcid.org/0000-0003-3556-6568>  
 Xiangrong Fu  <https://orcid.org/0000-0002-4305-6624>  
 Senbei Du  <https://orcid.org/0000-0003-1134-3909>

### References

- Andrés, N., Clark di Leoni, P., Mininni, P. D., et al. 2017, *PhPI*, **24**, 102314  
 Armstrong, J. W., Rickett, B. J., & Spangler, S. R. 1995, *ApJ*, **443**, 209  
 Bieber, J. W., Wanner, W., & Matthaeus, W. H. 1996, *JGR*, **101**, 2511  
 Brodiano, M., Andrés, N., & Dmitruk, P. 2021, *ApJ*, **922**, 240  
 Burlaga, L. F., Florinski, V., & Ness, N. F. 2018, *ApJ*, **854**, 20  
 Chandran, B. D. G. 2005, *PhRvL*, **95**, 265004  
 Chhiber, R., Matthaeus, W. H., Oughton, S., & Parashar, T. N. 2020, *PhPI*, **27**, 062308  
 Cho, J., & Lazarian, A. 2002, *PhRvL*, **88**, 245001  
 Cho, J., & Lazarian, A. 2003, *MNRAS*, **345**, 325  
 Clark di Leoni, P., Mininni, P. D., & Brachet, M. E. 2015, *PhRvA*, **92**, 063632  
 Cranmer, S. R., & Ballegoijen, A. A. V. 2012, *ApJ*, **754**, 92  
 Demidem, C., Lemoine, M., & Casse, F. 2020, *PhRvD*, **102**, 023003  
 Dermer, C. D., Miller, J. A., & Li, H. 1996, *ApJ*, **456**, 106  
 Diamond, P. H., Itoh, S. I., Itoh, K., & Hahm, T. S. 2005, *PPCF*, **47**, R35  
 Dmitruk, P., & Matthaeus, W. H. 2007, *PhRvE*, **76**, 036305  
 Dmitruk, P., & Matthaeus, W. H. 2009, *PhPI*, **16**, 062304  
 Eswaran, V., & Pope, S. B. 1988, *CF*, **16**, 257  
 Galtier, S. 2009, *NPGeo*, **16**, 83  
 Galtier, S. 2018, *JPhA*, **51**, 293001  
 Goldreich, P., & Sridhar, S. 1995, *ApJ*, **438**, 763  
 Harris, F. J. 1978, *IEEEP*, **66**, 51  
 Hitomi Collaboration, Aharonian, F., Akamatsu, H., et al. 2018, *PASJ*, **70**, 9  
 Li, H., & Miller, J. A. 1997, *ApJL*, **478**, L67  
 Lugones, R., Dmitruk, P., Mininni, P. D., Pouquet, A., & Matthaeus, W. H. 2019, *PhPI*, **26**, 122301  
 Makwana, K. D., & Yan, H. 2020, *PhRvX*, **10**, 031021  
 Markovskii, S. A., & Vasquez, B. J. 2020, *ApJ*, **903**, 80  
 Marsch, E. 1986, *A&A*, **164**, 77  
 Matthaeus, W. H., & Goldstein, M. L. 1982, *JGR*, **87**, 6011  
 Meyrand, R., Galtier, S., & Kiyani, K. H. 2016, *PhRvL*, **116**, 105002  
 Miller, J. A., Larosa, T. N., & Moore, R. L. 1996, *ApJ*, **461**, 445  
 Schlickeiser, R. 2002, *Cosmic Ray Astrophysics* (Berlin: Springer), 519  
 Stone, J. M., Tomida, K., White, C. J., & Felker, K. G. 2020, *ApJS*, **249**, 4  
 Svidzinski, V. A., Li, H., Rose, H. A., Albright, B. J., & Bowers, K. J. 2009, *PhPI*, **16**, 122310  
 Yan, H., & Lazarian, A. 2002, *PhRvL*, **89**, 281102  
 Yang, L., Zhang, L., He, J., et al. 2018, *ApJ*, **866**, 41  
 Yang, L. P., Li, H., Li, S. T., et al. 2019, *MNRAS*, **488**, 859  
 Zank, G. P., Adhikari, L., Hunana, P., et al. 2017, *ApJ*, **835**, 147  
 Zank, G. P., Du, S., & Hunana, P. 2017, *ApJ*, **842**, 114  
 Zank, G. P., & Matthaeus, W. H. 1992, in *Proc. of the 3rd COSPAR Coll., Solar Wind Seven* (Oxford: Pergamon), 587  
 Zank, G. P., & Matthaeus, W. H. 1993, *PhFIA*, **5**, 257  
 Zank, G. P., Nakanotani, M., & Webb, G. M. 2019, *ApJ*, **887**, 116  
 Zank, G. P., Nakanotani, M., Zhao, L.-L., Adhikari, L., & Telloni, D. 2020, *ApJ*, **900**, 115  
 Zhang, L., He, J., Tu, C., et al. 2015, *ApJL*, **804**, L43  
 Zhao, L. L., Zank, G. P., & Burlaga, L. F. 2020, *ApJ*, **900**, 166  
 Zhao, L. L., Zank, G. P., He, J. S., et al. 2021, *ApJ*, **922**, 188